International Journal of Nanomedicine

Dovepress
open access to scientific and medical research

Open Access Full Text Article

ORIGINAL RESEARCH

TME-Responsive Nanoplatform with Glutathione Depletion for Enhanced Tumor-Specific Mild Photothermal/Gene/Ferroptosis Synergistic Therapy

Yuhang Tian[1], Xiang He[1], Yanchi Yuan[1], Shijie Zhang[2], Chunyue Wang[1], Jialin Dong[1], Zhao Liu[1], Hui Jing[1]

[1]Department of Ultrasound, Harbin Medical University Cancer Hospital, Harbin, 150081, People's Republic of China; [2]Department of Radiation Oncology, Harbin Medical University Cancer Hospital, Harbin, 150081, People's Republic of China

Correspondence: Hui Jing, Department of Ultrasound, Harbin Medical University Cancer Hospital, 150 Haping Road, Nangang District, Harbin, 150081, People's Republic of China, Email jinghuihrb@163.com

Background: Triple negative breast cancer (TNBC) is one of the worst prognosis types of breast cancer that urgently needs effective therapy methods. However, cancer is a complicated disease that usually requires multiple treatment modalities.

Methods: A tumor microenvironment (TME)-responsive PFC/TRIM37@Fe-TA@HA (abbreviated as PTFTH) nanoplatform was constructed by coating Fe^{3+} and tannic acid (TA) on the surface of TRIM37-siRNA loaded phase-transition perfluorocarbon (PFC) nanodroplets and further modifying them with hyaluronic acid (HA) to achieve tumor-specific mild photothermal/gene/ferroptosis synergistic therapy (MPTT/GT/ Ferroptosis) in vitro. Once internalized into tumor cells through CD44 receptor-mediated active targeting, the HA shell of PTFTH would be preliminarily disassembled by hyaluronidase (HAase) to expose the Fe-TA metal-phenolic networks (MPNs), which would further degrade in response to an acidic lysosomal environment, leading to HAase/pH dual-responsive release of Fe^{3+} and PFC/TRIM37.

Results: PTFTH showed good biocompatibility in vitro. On the one hand, the released Fe^{3+} could deplete the overexpressed glutathione (GSH) through redox reactions and produce Fe^{2+}, which in turn converts endogenous H_2O_2 into highly cytotoxic hydroxyl radicals (•OH) for chemodynamic therapy (CDT). On the other hand, the local hyperthermia generated by PTFTH under 808 nm laser irradiation could not only improve CDT efficacy through accelerating the Fe^{2+}-mediated Fenton reaction, but also enhance TRIM37-siRNA delivery for gene therapy (GT). The consumption of GSH and accumulation of •OH synergistically augmented intracellular oxidative stress, resulting in substantial tumor cell ferroptosis. Moreover, PTFTH possessed outstanding contrast enhanced ultrasound (CEUS), photoacoustic imaging (PAI) and magnetic resonance imaging (MRI) ability.

Conclusion: This PTFTH based multiple-mode therapeutic strategy has successfully achieved a synergistic anticancer effect in vitro and has the potential to be translated into clinical application for tumor therapy in future.

Keywords: mild photothermal therapy, gene therapy, ferroptosis, synergistic therapy, multimodal imaging

Introduction

Breast cancer is the most common invasive female tumor and the second leading cause of death.[1] TNBC, with negative expression of progesterone receptor (PR), estrogen receptor (ER), and human epidermal growth factor receptor 2 (HER2), accounts for about 15%-20% of all breast cancer cases.[2] Due to extreme aggressive phenotype, high recurrence rates, high distant metastasis rate, TNBC has extremely poor prognosis.[3] Due to the lack of targeted therapy, chemotherapy is the only usable systemic therapy. Even though TNBC patients can benefit from standard chemotherapeutic regimen, they still face high rates of recurrence and high possibility of drug resistance[4]. Hence, it is very necessary to seek a novel therapeutic approach for effective tumor therapy.[5–7]

Ferroptosis is an iron-dependent and non-apoptotic form of programmed cell death characterized by dysregulation of lipid peroxidation.[8] Distinguishing itself from apoptosis, necrosis, and autophagy, ferroptosis results in the imbalance of

Received: 25 June 2024
Accepted: 28 August 2024
Published: 6 September 2024

oxidation-reduction levels in tumor cells via dysregulated iron accumulation and iron metabolism.[9] Research shows that two main mechanisms trigger ferroptosis: (1) direct consuming the cellular antioxidant GSH,[10] (2) inhibiting the activity of Glutathione Peroxidase 4 (GPX4), responsible for reducing lipid oxidation.[11,12] With an in-depth understanding of the mechanism, ferroptosis has been extensively researched as a potential therapeutic strategy to ruin tumors and overcome the deficiencies of apoptosis-mediated conventional therapies. However, tumor cells possess a special oxidative stress defense system via endogenous antioxidants, such as GSH. Therefore, it is highly necessary to push the redox balance in tumor cells towards a more oxidative state for effective tumor treatment.[13–16] Recently, augmented oxidative tumor cells damage has been realized by combining GSH consumption with reactive oxygen species (ROS) generating CDT.[17]

GT is recognized to be a secure and effective treatment applying exogenous nucleic acids as therapeutic agents, and has the potential to restrain oncogenes and inhibit the proliferation of tumors.[18–20] Small interfering RNA (siRNA), as an effective mediator of RNA interference, can mediate posttranscriptional gene silencing. Nevertheless, its therapeutic efficiency is not entirely satisfactory due to the limitations of naked siRNA, for instance, inferior transfection efficiency, easy enzymatic degradation, inefficient endosomal escape, and nonspecific biodistribution.[21] Therefore, the successful implementation of GT requires the utilization of delivery vector that can efficiently overcome above biological barriers.

Some researchers have reported that ultrasound targeted microbubble destruction (UTMD) mediated gene delivery could enhance gene expression, especially when using cationic microbubbles with comparatively high gene carrying ability and effective endosomal escape.[22,23] However, microbubbles are usually micron-sized, preventing them from passing through the gaps of the tumor blood vessels. In addition, with sonication instability and intolerance to physics distortion, the gas-phase perfluorocarbon microbubbles possess a short circulation time in vivo.[24] Hence, PFC nanodroplets, in which the liquid inside of the nanodroplets vaporizes to gas phase upon ultrasound or laser exposure, were served as substitution.[25–27] The PFC nanodroplets keep stable in liquid phase until they are triggered to vaporization for gene delivery. The triggering of the PFC nanodroplets into gas phase was traditionally implemented using ultrasound irradiation with a relatively high-pressure amplitude, referred to as acoustic droplet vaporization (ADV).[28,29] However, it's quite difficult to trigger vaporization by ultrasound due to Laplace pressure of the droplet and the function of surface stabilizing agents.[30] Optically-triggered phase-transition techniques, also known as optical droplet vaporization (ODV), have been proved to be an effective substitution for activation of PFC nanodroplets, through integration of optical absorbing substance and the liquid core.[31]

Tripartite motif containing protein 37 (TRIM37) has been reported as an oncogenic histone H2A ubiquitin ligase that is overexpressed in a portion of breast cancers.[32] TRIM37 was considered to be associated with chemotherapy resistance and metastasis of TNBC in vitro and in vivo studies.[33] Clinically, TRIM37 over-expression is associated with poor prognosis. Functionally, high-TRIM37 induces non-transformed breast cells tumorigenic, and inhibition of TRIM37 action decreases tumor growth.[32]

Herein, we designed a TME-activated and near infrared (NIR)-driven nanoplatform with the ability of providing a feasible approach for the treatment of TNBC (Scheme 1). In our formulation, The PFC nanodroplets with cationic charge were selected as the gene carrier to efficiently load TRIM37-siRNA, and then Fe-TA MPNs were coupled into their surface to form PFC/TRIM37@Fe-TA (abbreviated as PTFT). In order to improve the targeting ability, PTFT was further decorated with HA, leading to a novel nanoplatform PFC/TRIM37@Fe-TA@HA (abbreviated as PTFTH). Once injected into tumor-bearing mice through the tail vein, PTFTH could selectively accumulate at tumor sites via the enhanced permeability and retention (EPR) effect and HA-mediated active targeting. Following endocytosis into tumor cells, the external HA coating would be firstly disassembled by HAase to reveal the Fe-TA MPNs, which would be further degraded in answer to an acidic lysosomal environment, resulting in the HAase/pH-triggered release of Fe^{3+} and PFC/TRIM37. The released Fe^{3+} could be converted to Fe^{2+} by TA and then catalyze endogenously overexpressed H_2O_2 to generate cytotoxic •OH for CDT and further use up the intracellular GSH. Subsequently, under laser exposure, ODV mediated gene transfection could enhance TRIM37 delivery and the PFC offer superior ultrasound contrast, once the liquid core was triggered into gaseous phase. In addition, the Fe-TA MPNs possess the potency of PAI and T_1-MRI.[34] Meanwhile, the Fe-TA MPNs with excellent photothermal conversion efficiency could effectively convert the NIR light into heat for mild photothermal therapy (MPTT). Notably, MPTT not only accelerated the Fe^{2+}-mediated Fenton

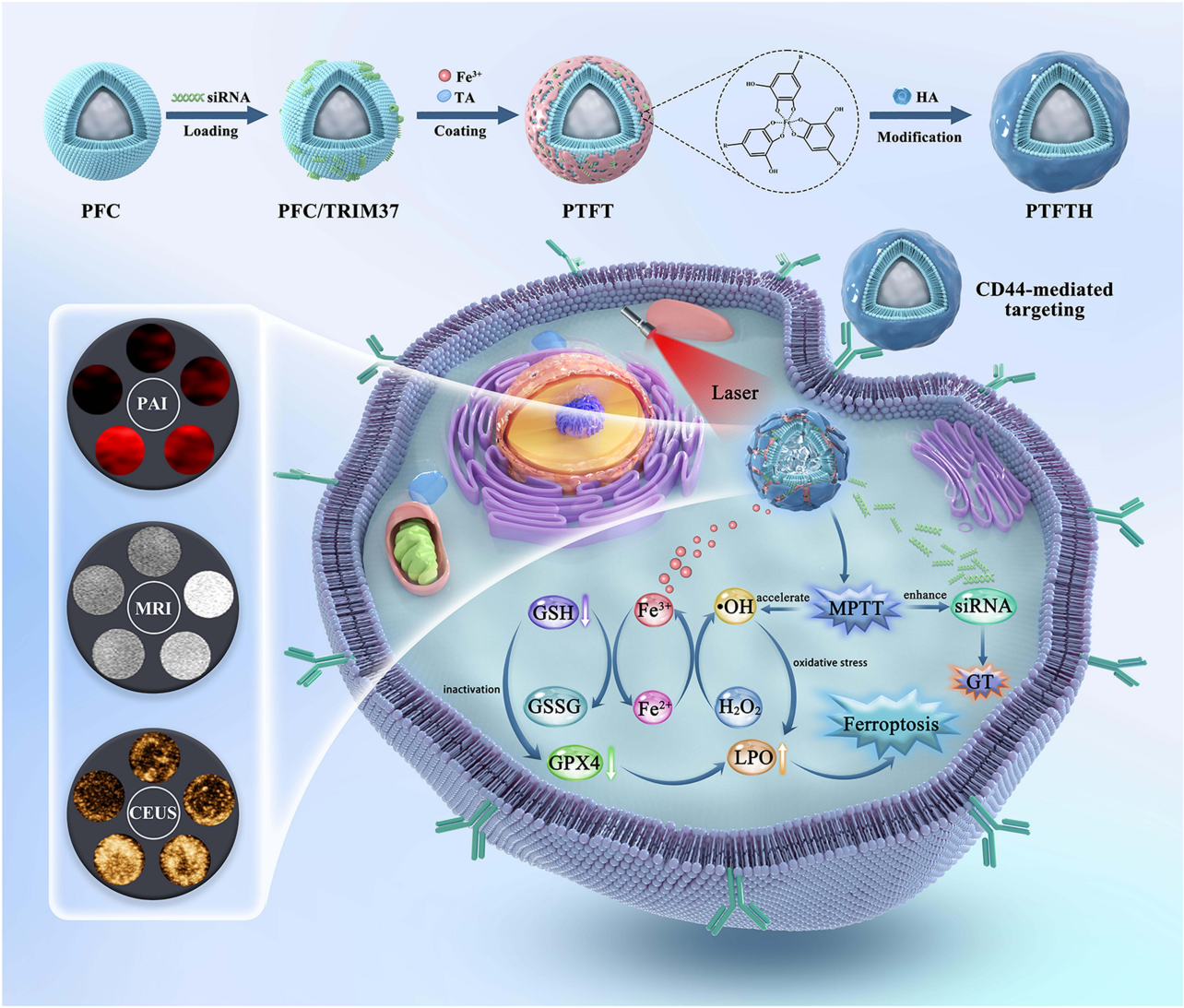

Scheme 1 Schematic illustration of the synthetic procedure of PTFTH and its underlying mechanism for mild photothermal/gene/ferroptosis synergistic therapy.

reaction,[35] but also enhanced cellular uptake and accelerated gene release,[36] achieving mutually synergistic therapy of MPTT, CDT and GT.

Materials and Methods

Preparation of the Cationic PFC Nanodroplets

The thin-film hydration and ultrasonic emulsification method were used to prepare the cationic PFC nanodroplets which were reported in the previous research.[37] Distearoylphospha-tidylcholine (DSPC), 1.2-distearoyl-sn-glycero-3-phosphoethanolamine-N-(methoxy(polyethylene glycol)-2000 (DSPE-PEG2000) and 3-(N-(N′,N′-dimethyl-laminoethane)-carbamoyl-cholesterol (DC-CHOL) were mixed at a weight ratio of 5:2:2 (See "Materials" for more details). Next, the mixture was dissolved in chloroform and evaporated on a rotary vacuum evaporator (Shyarong, China) at 50 ˚C for 2 h to remove the organic solvent. Then, a lipid film was obtained and hydrated in PBS. Subsequently, 100 μL perfluoropentane (PFP) was dropped into the lipid film and emulsified using a sonicator with a power of 125 W for 5 min. Finally, the cationic PFC nanodroplets were harvested after being centrifuged. To prepare fluorescent nanodroplets, 1 mg of 1.1-dioctadecyl-3,3,3,3-tetramethylindocarbocyanine perchlorate (DiI) fluorescent dye was added to the lipid solution.

TRIM37-siRNA Construction

The TRIM37-siRNA was designed and compared with the human genome database (National Center for Biotechnology Information, NCBI). TRIM37-siRNA labeled by 5-Carboxy fluorescein (FAM) was synthesized by HanBio (Shanghai, China). Table S1 shows the TRIM37-siRNA sequences.

Preparation of PTFTH

The TRIM37-siRNA loaded PFC complex (PFC/TRIM37) were fabricated by mixing the cationic PFC nanodroplets with FAM labeled TRIM37-siRNA at different ratios and incubated for 30 min at room temperature to obtain PFC/TRIM37 via electrostatic adsorption. After that, the mixture was centrifuged at 10,000 rpm for 10 min. PFC/TRIM37@Fe-TA was prepared by dispersing 1 mg of PFC/TRIM37 into 2 mL of ultrapure water and followed by adding TA solution (10 μL, 40 mg/mL) and $FeCl_3$ solution (20 μL, 10 mg/mL) under vortex. Subsequently, the solution pH was adjusted to ~7.0 using NaOH solution (0.1 mol/L). The products were centrifuged to acquire PTFT, and rinsed with ultrapure water. Afterward, the obtained PTFT was added into 5 mL of HA solution and stirred for 8 h. Finally, the as-prepared PTFTH was purified with ultrapure water, and then sterilized by ^{60}Co-γ radiation and stored at 4 °C for future use.

Estimation of siRNA Attaching to Nanodroplets

siRNA was loaded onto the as-prepared PFC nanodroplets based on electrostatic adsorption. In short, different amounts (volume ratios of 5:1, 10:1, 15:1, 20:1, 25:1, and 30:1) of the as-synthesized nanodroplets were added to the siRNA solution and incubated for 30 min. Then, the binding of siRNA to nanodroplets was determined by 2% agarose gel electrophoresis containing GelRed. To evaluate the release of siRNA from PFC/TRIM37, various volume ratios of PFC/TRIM37 were synthesized as mentioned above. All the samples were blended with 2% sodium dodecyl sulfate (SDS) and then electrophoresed on agarose gel after incubation for 10 min at room temperature. To demonstrate the stability of the loaded siRNA, RNase was added to the as-synthesized PFC/TRIM37 solution and incubated at 37 °C for 1 h. The RNase was then inactivated with Diethyl pyrocarbonate (DEPC) and incubated for 10 min at room temperature. The mixture was then treated with SDS to extract undegraded siRNA and analyzed by agarose gel electrophoresis.

The cationic PFC nanodroplets labeled by DiI were blended with FAM-labeled siRNA and incubated for 30 min. After that, the solution was added to a RNAase-free centrifuge tube and centrifuged at 10000 rpm for 10 min to remove unbound siRNA. The precipitate obtained by centrifugation was resuspended with ultrapure water. Then, an appropriate amount of solution was dropped onto a glass slide and covered with a cover glass slide before fluorescence microscope (Leica, Wetzlar, Germany) observation.

In vitro Fe Release Kinetics

Responsive Fe release from PTFTH was tested under different pHs (6.0 and 7.4) with or without HAase (200 U/mL). First, PTFTH solution (1 mL, 1.0 mg/mL) was put into a dialysis bag with molecular weight cutoff (MWCO) of 500 Da, and the bag was placed in 9 mL of corresponding buffer medium. After that, the entire system was kept at 37 °C to vibrate. Then, 1 mL of the outer phase buffer medium was removed at each scheduled time interval, and measured by Inductively Coupled Plasma Optical Emission Spectrometer (ICP-OES, Optima 8000), meanwhile the equal volume of the corresponding buffer medium was added into the outer phase.

Measurement of GSH Consumption

Different concentrations of PTFTH (50, 100, 200 and 400 μg/mL) were dispersed in PBS solution (pH 6.0), followed by blending with GSH solution (1 mM) and incubated for 2 h at room temperature. After centrifugation, 5.5′-dithiobis (2-nitrobenzoic acid) (DTNB) solution was added into the supernatant and the absorbance of the compound was recorded by using UV-vis spectrophotometer (Perkin Elmer, Waltham, MA).

Detection of •OH Generation

Based on the oxidation of methylene blue (MB), a colorimetric method was used to determine the •OH generation ability of PTFTH. Briefly, PTFTH was divided into the following four groups: A: 0 mM GSH; B: 1 mM GSH; C: 2 mM GSH; D: 2 mM GSH + L. For the first three groups, PTFTH was dispersed into 3 mL of phosphate buffer (pH 6.0) containing different concentrations of GSH (0, 1, 2 mM) and shaken for 1 h at room temperature. After centrifugation, the supernatant was blended with MB (10 μg/mL) and H_2O_2 (10 mM) and incubated for 15 min. Then, the UV-vis spectrophotometer was used to record the absorbance of each compound at 665 nm, and reflect the •OH-induced degradation of MB. For group D, the difference was that the supernatant was blended with MB and H_2O_2, combining with laser (808nm, 1.0 W/cm^2, 5min) irradiation. Subsequently, the •OH generation ability of PTFTH was further studied under different pHs (6.0 and 7.4). PTFTH was similarly dispersed into 3 mL of phosphate buffer with different pHs (6.0 and 7.4) containing MB (10 μg/mL) and H_2O_2 (10 mM), followed by incubation at room temperature for 1 h. Then, the •OH-induced MB degradation was monitored by UV-vis spectrophotometer. As a contrast, the MB solution and MB/H_2O_2 mixture solution were also detected under equal conditions.

In vitro Photothermal Test

PTFTH suspensions were added into 96-well plates and their thermal characteristics were measured under 808 nm laser irradiation at different irradiation intensities (0.5, 1.0, 1.5, and 2.0 W/cm^2), with elevated concentrations (50, 100, 200, and 400 μg/mL) for 10 min. The ultrapure water was used as control under the same conditions. To evaluate the effective ingredients of photothermal capacities, 200 μL of sample solution of PTFTH, Fe-TA, $FeCl_3$, and TA with equal concentration was added into 96-well plates and their thermal characteristics were measured under 808 nm laser irradiation at 2.0 W/cm^2 for 10 min. The temperature changes at different time intervals were recorded by a NIR camera (E6, FL-IR Systems, Inc, USA). To test the photothermal stability of PTFTH, PTFTH was exposed to 808 nm laser irradiation for five heating and cooling cycles.

Gene Transfection Assay in vitro

MDA-MB-231 cells were seeded onto 6-well plates and divided into 6 groups: (1) control, (2) TRIM37-siRNA, (3) TRIM37-siRNA + L, (4) PFC/TRIM37 + L, (5) PTFT + L, (6) PTFTH + L. For irradiation group, the cells were subjected to an 808 nm laser (1.0 W/cm^2) for 5 min. The cells were then divided into three groups for fluorescence microscope observation, PCR and Western blot staining, respectively. At 24 h after treatment, the intracellular distribution of FAM fluorescence was detected by fluorescence microscope.

At 48 h after treatment, the TRIM37-mRNA levels of the MDA-MB-231 cells were evaluated by using real time quantitative PCR (RT-qPCR). Total RNA was extracted with the high pure RNA isolation kit, and the total RNA was transcribed into cDNA using the All-in-one First Strand cDNA Synthesis Kit. RT-qPCR was performed with the SYBR Master Mix. Table S2 shows the primer sequences for TRIM37 and β-actin.

At 72 h after treatment, the MDA-MB-231 cells were collected, lysed, and then proteins were extracted and quantified by BCA assay. Samples were separated on 12.5% polyacrylamide gel and transferred to a nitrocellulose filter membrane, which was blocked with 5% skimmed milk and incubated overnight at 4 °C with primary antibodies, including TRIM37 and GAPDH. After washing three times and incubating with the secondary antibodies, the protein bands were observed using enhanced chemiluminescence detection. Quantitative analysis of protein was carried out using ImageJ software.

Cellular Uptake Assay

The cellular uptake of different nanocomplexes in MDA-MB-231 cells or MCF-10A cells were checked to investigate the targeting ability of HA-coated nanocomplexes. MDA-MB-231 cells or MCF-10A cells were seeded onto 24 well plates at a density of 10^5 cells per well and incubated for 24 h. After that, the culture medium in each well was substituted with fresh medium containing DiI-labeled PTFT or DiI-labeled PTFTH, and incubated for 4 h. Then, the culture medium was taken out and cells were washed with PBS for three times, and stained with DAPI for 15 min before fluorescence microscope observation.

Evaluation of Lysosomal Escape Capability

MDA-MB-231 cells were planted into confocal dishes at a density of 10^5 cells per dish and cultured for 24 h. Subsequently, the culture medium was replaced by fresh medium containing FAM-labeled PTFTH. After incubation for various time intervals (1 and 4 h), the cells were washed with PBS for three times and dyed with LysoTracker Red for 20 min. Next, the cells were fixed in 4% paraformaldehyde and incubated with DAPI for nucleus staining. The fluorescence images were visualized by confocal laser scanning microscopy (CLSM, Carl Zeiss LSM 700, Jena, Germany), and the co-localization analysis was achieved using ImageJ software.

Intracellular GSH, GPX4, and MDA Assay

MDA-MB-231 cells in 6 well plates (5 x 10^5 cells per well) were cultured overnight and treated with (1) Control, (2) PFC/TRIM37, (3) Fe-TA, (4) PTFT, (5) PTFTH, and (6) PTFTH + L for 4 h. For irradiation group, the cells were then subjected to an 808 nm laser (1.0 W/cm^2) for 5 min. After another incubation for 8 h, the GSH amount was monitored using GSH and GSSG Assay Kit; the GPX4 activity was evaluated using Glutathione peroxidase assay kit; the Malondialdehyde (MDA) amount was measured using MDA assay kit. In addition, BCA protein assay kit was used to assay the protein concentration of cellular samples.

Intracellular Free Radical Measurement

MDA-MB-231 cells were seeded onto 24-well plates (10^5 cells per well) and cultured for 24 h. Subsequently, these cells were subjected to the equal treatment as described in the GSH Assay and dyed with 2′,7′-dichlorodihydrofluorescein diacetate (DCFH-DA) for 30 min. Finally, the fluorescence of DCF was analyzed by fluorescence microscope.

Cell Cytotoxicity Assay

CCK-8 assay was used to investigate the cytotoxicity of different nanocomplexes. First of all, to evaluate the effect of CDT induced by Fe-TA and GT induced by TRIM37-siRNA on breast cancer cells or breast normal cells, MDA-MB-231 cells or MCF-10A cells were seeded onto 96 well plates at a density of 10^4 cells per well and incubated for 24 h. Next, the culture medium for each well was replaced with fresh medium containing PTFT or PTFTH at different concentrations (50, 100, 200, and 400 μg/mL, respectively) and incubated for another 24 h. After that, the cells were washed with PBS for three times and incubated with 100 μL serum-free medium containing 10 μL CCK-8 for 1 h. At last, the absorbance of each well at 450 nm was measured by a microplate reader (Promega Corp, Madison, WI, USA).

Subsequently, to test the therapeutic efficacy of TRIM37-siRNA induced GT and the cooperative effect of Fe-TA and TRIM37-siRNA, the cytotoxicity of PFC/TRIM37, Fe-TA, PTFT, PTFTH, and PTFTH + L was evaluated through CCK-8 assay as described above (n = 3). For irradiation group, the cells were exposed to an 808 nm laser (1.0 W/cm^2) for 5 min.

Live/Dead Cell Staining Assay

MDA-MB-231 cells in 24 well plates (10^5 cells per well) were cultured overnight and treated with (1) Control, (2) PFC/TRIM37, (3) Fe-TA, (4) PTFT, (5) PTFTH, and (6) PTFTH + L for 4 h. For irradiation group, the cells were then subjected to an 808 nm laser (1.0 W/cm^2) for 5 min. After incubating for 20 h, the cells were stained with Calcein-AM and propidium iodide (PI). Finally, the cells were washed with PBS for three times and observed by fluorescence microscope.

In vitro Multi-Mode Imaging Capability

An agar gel mold was applied to evaluate the function of PTFTH as an ultrasound contrast agent in vitro. The ultrasound images of PTFTH at various concentrations (100, 200, 300, 400 and 500 μg/mL) were investigated in the contrast-mode using Resona R9 (Mindray, China). After PTFTH was exposed to 808nm laser at 1W/cm^2 for 5min, CEUS images were captured for different groups.

To study PAI property of PTFTH, PTFTH with different concentrations ranging from 25 μg/mL to 150 μg/mL were investigated using a Vivo LAZR photoacoustic (PA) imaging system (VisualSonics, Toronto, Canada).

T_1-weighted imaging in vitro was conducted on a Bruker BioSpec 9.4T MR scanner (Bruker, Ettlingen, Germany). For in vitro imaging, different concentrations of PTFTH were prepared and sealed in centrifuge tubes for test. Concentration of Fe element was determined by ICP.

Statistical Analysis

All data were expressed as mean ± standard deviation (SD). The data were analyzed using SPSS 20.0 software. A one-way ANOVA was applied to analyze the significance among groups' data (*p < 0.05, **p < 0.01, ***p < 0.001, ****p < 0.0001).

Results and Discussion

Preparation and Characterization of PTFTH

The cationic PFC nanodroplets were first prepared via thin-film hydration and ultrasonic emulsification method.[37] Then, TRIM37-siRNA labeled by FAM was linked via electrostatic adsorption. The most critical factors to consider when preparing a siRNA delivery system are the binding ability, stability, and release of siRNA. In order to evaluate the binding affinity of siRNA to the cationic PFC nanodroplets, agarose gel electrophoresis was performed using nanodroplets and siRNA at various volume ratios (5:1 to 30:1). The migration of PFC/TRIM37 was prevented at volume ratios higher than 25 (Figure 1d), indicating that the binding between the vector and the siRNA was powerful enough to resist

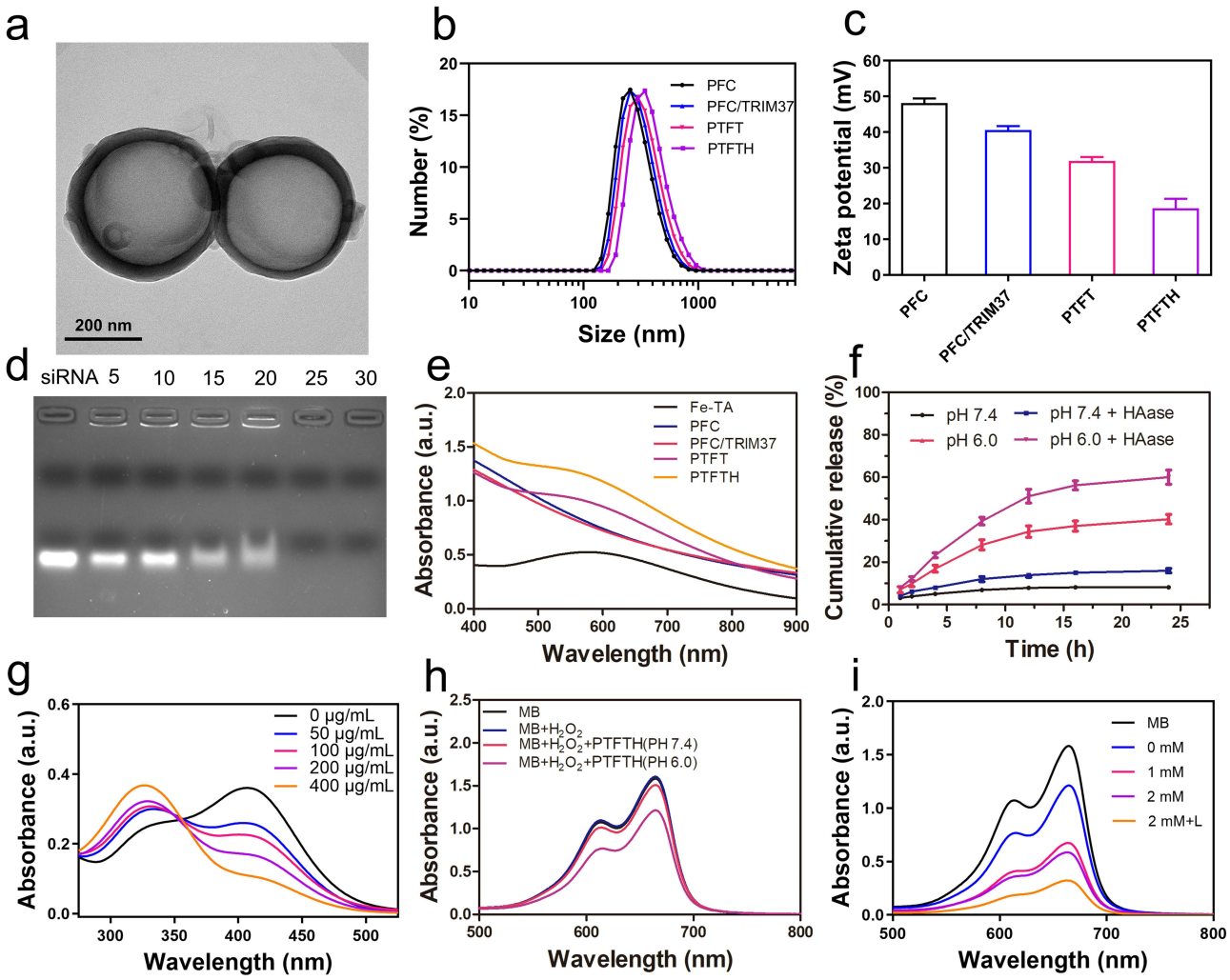

Figure 1 (**a**) TEM image of PTFTH, (**b**) size distributions and (**c**) Zeta potentials of PFC, PFC/TRIM37, PTFT, and PTFTH. (**d**) Agarose gel retardation assay of PFC/TRIM37 complexes under various volume ratios (5:1, 10:1, 15:1, 20:1, 25:1, and 30:1). (**e**) UV-vis absorption spectra of PFC, PFC/TRIM37, Fe-TA complex, PTFT, and PTFTH. (**f**) Accumulated release profiles of Fe from PTFTH under different conditions. (**g**) GSH depletion by different concentrations of PTFTH at pH 6.0. (**h** and **i**) UV-vis absorption spectra of MB after treatment with different samples (MB: 10 μg/mL, H_2O_2: 10 mM).

dissociation during electrophoresis. Hence, a volume ratio of 25:1 was selected for further experiments. The stability and release of PFC/TRIM37 complexes were then assessed by RNAse digestion followed by SDS substitution. The SDS treatment leads to the release of siRNA from the PFC/TRIM37 (Figure S1a). In Figure S1b, the band for naked siRNA sample is lost, demonstrating that the siRNA was degraded by the RNAse. On the contrary, the PFC/TRIM37 complexes show visible bands, indicating that the siRNA was protected from degradation due to association with the carrier. Subsequently, fluorescence microscope images of PFC/TRIM37 showed that the TRIM37-siRNA was labeled by FAM with green fluorescence and the lipid membrane of PFC was stained with red fluorescence (Figure S2). The wide overlap of red and green fluorescence proves the successful attachment between the TRIM37-siRNA and the PFC nanodroplets.

TA, a familiar natural polyphenol with multiple chelation ability, can coordinate with various metal irons into a three-dimensional network within a few seconds. Using PFC/TRIM37 as a template, TA and Fe^{3+} aqueous solution was sequentially added into the PFC/TRIM37 solution to form the Fe-TA MPNs on the surface of template followed by pH neutralization. A black color suspension appeared after the addition of TA and Fe^{3+} aqueous solution, while an ivory-white color in the suspension of PFC/TRIM37 (Figure S3). The instant change in appearance indicates the complexation between TA and Fe^{3+} aqueous solution, forming a shell enclosing the PFC/TRIM37. To further verify the coating results, UV-vis absorption spectra were performed to detect the Fe-TA MPNs. In comparison to PFC and PFC/TRIM37, characteristic absorbance peaks at around 560–600 nm in both Fe-TA complex, PTFT, and PTFTH were observed (Figure 1e), indicating the success formation of the Fe-TA MPNs.[38] Inductively coupled plasma (ICP) indicated that the Fe encapsulation efficiency was 41.2%. Eventually, HA as the tumor-targeting section was modified on the surface of PTFT to produce the final PTFTH. Transmission electron microscopy (TEM) images (Figures 1a and S4) presented the spherical morphology of PFC, PFC/TRIM37, PTFT and PTFTH. The stepwise synthesis process of PTFTH was confirmed by zeta potential analysis. As shown in Figure 1c, the initial zeta potential of PFC was +48.1 mV because of the existence of positively charged DC-CHOL, and ulteriorly reduced to +40.6 mV due to the connection of negatively charged siRNA. After coating with the Fe-TA MPNs, the zeta potential of PTFT adjusted to +31.9 mV and ultimately decreased to +18.7 mV after HA adhesion, indicating the successful attachment of carboxyl-containing HA. In addition, the results of dynamic light scattering (DLS) revealed a rational increase in the average particle size from 384.1 nm for PFC to 438.2 nm for PTFTH (Figure 1b). Such a size around 438 nm was more than enough for PTFTH to pass through the endothelial cell and locate at the tumor site. Besides, the particle size of PTFTH in PBS barely changed during the 9 days, further manifesting the excellent stability of PTFTH for potential biomedical applications (Figure S5). Furthermore, Figure S6 show the morphology characteristics of PTFTH before and after laser irradiation. It can be seen that the size of some PTFTH nanoparticles significantly increased after laser irradiation owing to the PFP liquid-gas phase transition. These findings lay foundation for the further use of PTFTH in CEUS imaging applications.

To validate whether Fe^{3+} could be released from PTFTH as a result of TME-specific stimulation, the biodegradation behavior of PTFTH with or without HAase at different pHs (6.0 and 7.4) was tested. As displayed in Figure 1f, negligible release of Fe^{3+} was observed in the presence or absence of HAase at pH 7.4. Contrastingly, the cumulative release of Fe^{3+} at pH 6.0 reached 40.2% after 24 h and further significantly increased to 60% with the addition of HAase, which may be attributed to the accelerated pH-induced degradation of the Fe-TA MPNs following HAase-mediated HA disassembly, thus facilitating the diffusion of Fe^{3+}.

Since the released Fe^{3+} could be converted into Fe^{2+} by GSH, the capacity of PTFTH to consume GSH was first detected via DTNB method, which could react with GSH to form the yellow TNB. As exhibited in Figure 1g, the absorbance peak of TNB at 412 nm declined gradually with the increasing concentration of PTFTH, suggesting that the GSH was effectively depleted by PTFTH. Inspired by the fact that the Fe^{2+} could catalyze H_2O_2 to generate •OH via Fenton reaction, we subsequently evaluated the •OH generation capacity of PTFTH by using MB as an indicator. Compared with the MB and "MB + H_2O_2" groups, the absorbance of MB decreased after incubation with PTFTH and H_2O_2 at pH 6.0, indicating the generation of •OH (Figure 1h). Due to the finite release of Fe^{3+} in a neutral environment, there was only a slight decrease in the MB absorbance after the same treatment at pH 7.4. As illustrated in Figure 1i, the degradation of MB was facilitated with the GSH concentration increasing from 0 to 2 mM at pH 6.0. Surprisingly, the degradation of MB was ulteriorly enhanced with the GSH concentration of 2 mM when exposed to laser irradiation. Perhaps it can be explained by previous reports, when the temperature increases from 20 °C to 50 °C, Fenton reaction

rate is increased by up to 4-fold.[35,39,40] This also proved the great potential of combining photothermal effect with ROS generated by Fenton reaction for synergistic cancer therapy.

Photothermal Performance

A characteristic feature of PTFTH was their thermal effect under the NIR irradiation, which could be used to achieve mild photothermal therapy. The PTFTH dispersions at the various concentrations were continuously irradiated with 808 nm laser for 10 min. The photothermal curves reflected a concentration-dependent and time-dependent manner (Figure 2a). Following 10 min exposure with elevated laser power from 0.5 to 2.0 W/cm^2, the temperature rose from 37.2 °C to 67.4 °C. Moreover, the temperature increase could be finely enhanced with increased power intensity (Figure 2b). Meanwhile, photothermal imaging performance of various PTFTH concentrations and different laser power intensities were also presented (Figure 2g and h). These results provided convincing evidence that PTFTH could act as an efficient photothermal material for the ablation of the tumor. The photothermal performance of PTFTH encouraged us to further study the heating properties of various components, including PTFTH, TA solution, $FeCl_3$ solution and Fe-TA complex solution at the same concentration. Only PTFTH and Fe-TA showed a significant increase in temperature, contrary to the negligible variation for the other two groups (Figure 2c). Based on above results, we can speculate that the photothermal effect of PTFTH is strongly correlated with the formation of the Fe-TA MPNs.

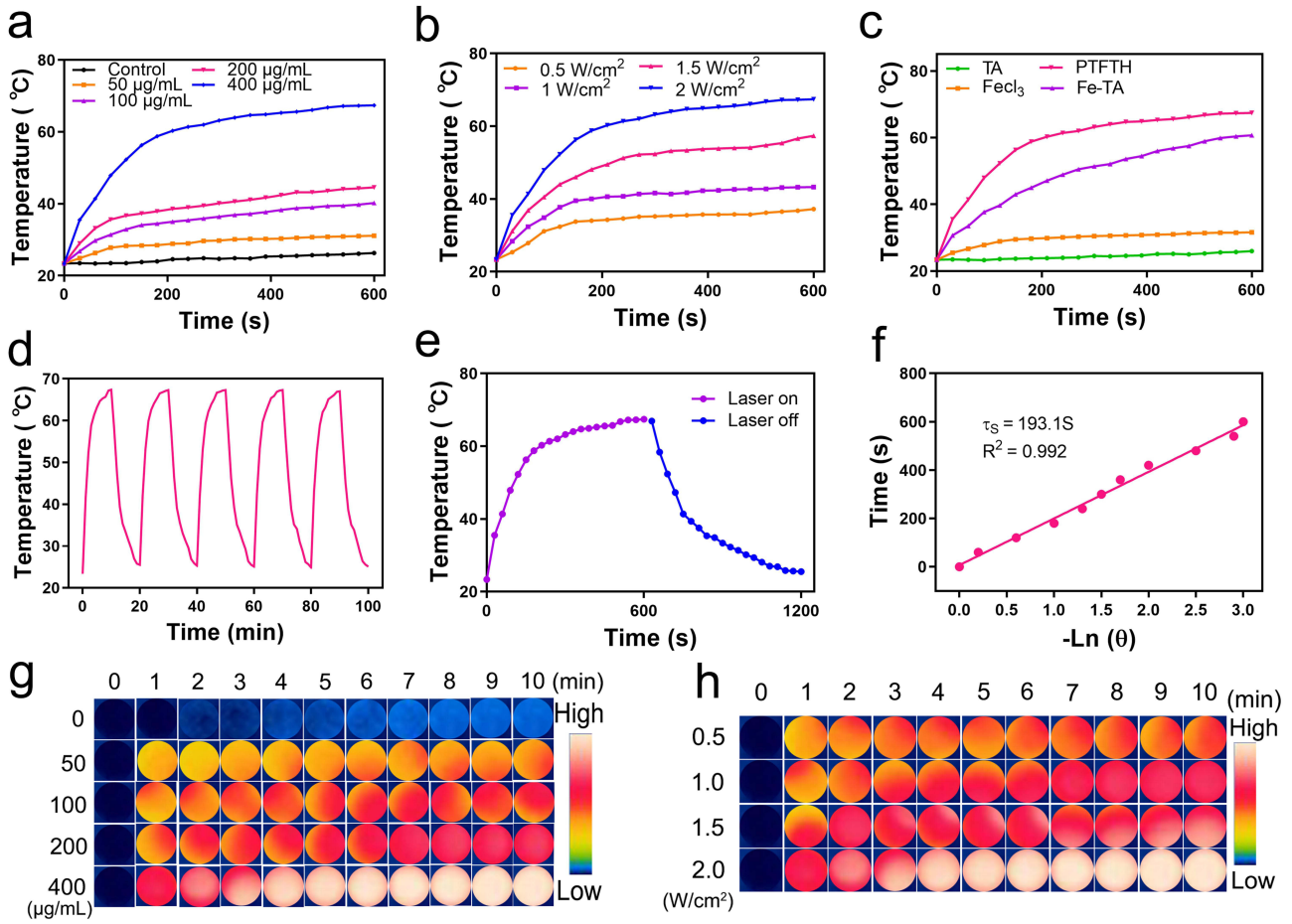

Figure 2 (**a**) Photothermal curves of PTFTH with 808 nm laser irradiation (2.0 W/cm^2, 10 min) at different concentrations (50, 100, 200, and 400 μg/mL). (**b**) Photothermal curves of PTFTH dispersed in aqueous solution irradiated with increased power densities (0.5, 1.0, 1.5 and 2.0 W/cm^2). (**c**) Photothermal curves of the aqueous dispersion of PTFTH, Fe-TA, TA, and $FeCl_3$. (**d**) Five heating and cooling cycles of PTFTH aqueous dispersion under 808 nm laser irradiation at the power intensity of 2.0 W/cm^2. (**e**) The temperature changes of PTFTH aqueous solution (400 μg/mL) under laser irradiation (808 nm, 2 W/cm^2) followed by the cooling period for 600 s. (**f**) The time constant for heat transfer obtained from the cooling curves. (**g**) Infrared thermal images with different concentrations of PTFTH in vitro. (**h**) Infrared thermal images with different laser power densities in vitro.

Furthermore, there was no significant attenuation on the photothermal effect of DFTNPs during five heating–cooling cycles, indicating satisfactory photothermal stability (Figure 2d).

Notably, the photothermal conversion efficiency (η) of PTFTH was calculated to be 36.6% (Figure 2e and f), which was much higher than previous reports,[41–43] suggesting that PTFTH could effectively convert the NIR laser energy into local heat for tumor treatment.

Gene Transfection in vitro

The transfection of siRNA was detected by fluorescence microscope. As shown in Figure 3a, there was no fluorescence in the control, TRIM37-siRNA, and "TRIM37-siRNA + L" groups, indicating that naked siRNA could not enter into tumor cells. While a few green fluorescence was found in the "PFC/TRIM37 + L" and "PTFT + L" groups, perhaps due to the mechanisms that the cationic PFC nanodroplets could guarantee siRNA loading capacity and laser irradiation could reversibly increase membrane permeability. In contrast, the green fluorescence in the "PTFTH + L" group was ulteriorly enhanced, which was ascribed to the active targeting of PTFTH to MDA-MB-231 cells. Furthermore, we also investigated the TRIM37 gene and protein expression in different groups by using RT-qPCR and Western blot (WB). The RT-qPCR and WB analyses indicate that the "PTFTH + L" group presented the least TRIM37 RNA and protein expression (Figure 3b and c). On the basis of the above results, the PTFTH could significantly enhance gene transfection upon laser irradiation.

Ultrasound targeted microbubble destruction (UTMD) mediated gene transfection has gained extensive attention in recent years.[44,45] The cavitation effect is considered the main effect of ultrasound that can be helpful in the process of gene delivery.[46] Cavitation is caused by microbubbles in response to acoustic excitation, and it could create strong shear pressure to enhance the cell permeability of tumor tissue, which can facilitate drugs or gene to enter cells through endocytosis.[47] In our study, when PTFTH arrived at the tumor sites, they were converted into micron-sized gas bubbles under laser exposure. The gas bubbles were then collapsed and produced cavitation effect to enhance cell permeability, similar to the principle of UTMD. All in all, the mechanism involved in laser irradiation mediated gene transfection was complicated. Further experiments are needed to elucidate the relevant mechanisms.

Cellular Uptake and Synergistic MPTT/GT/Ferroptosis in vitro

Considering the specific binding of HA with CD44 receptors overexpressed on the surface of tumor cells, the cellular uptake behaviors of PTFTH and PTFT in MDA-MB-231 cells and MCF-10A cells were respectively assessed by fluorescence microscope. As shown in Figure 4a, the PTFTH and PTFT were labeled by DiI with red fluorescence, and the nucleus of MDA-MB-231 and MCF-10A cells were stained with blue fluorescence. The wide overlap of red and

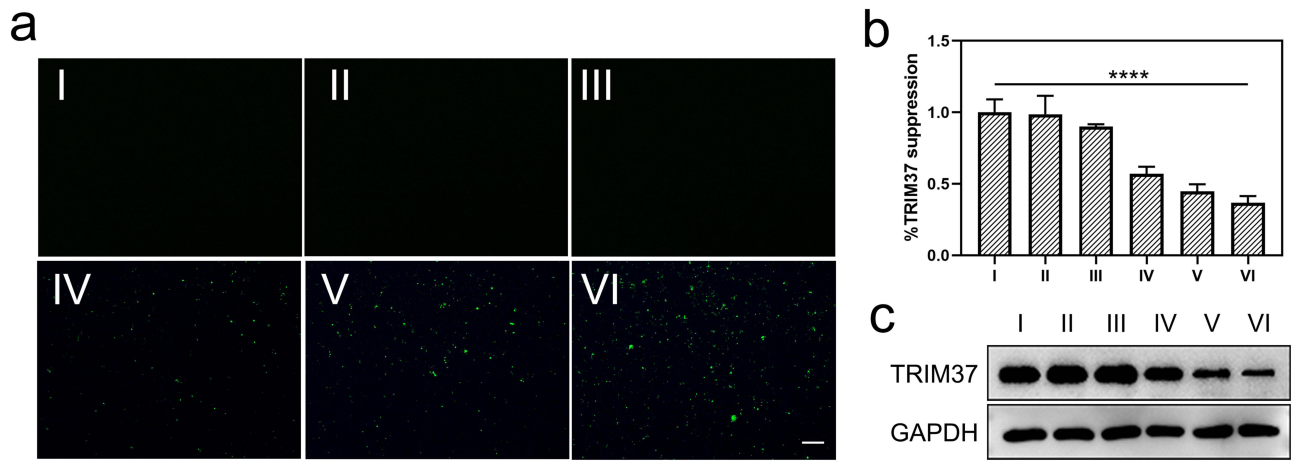

Figure 3 (**a**) Fluorescence images of MDA-MB-231 cells after transfection with FAM-labeled TRIM37-siRNA under different treatment conditions (scale bar: 100 μm). (**b**) RT-qPCR analysis of the expression levels of TRIM37. (**c**) Western blot of expression of TRIM37 in MDA-MB-231 cells. (I: Control, II: TRIM37-siRNA, III: TRIM37-siRNA + L, IV: PFC/TRIM37 + L, V: PTFT + L, VI: PTFTH + L. Data were presented as mean ± s.d. (n = 3). ****p < 0.0001.

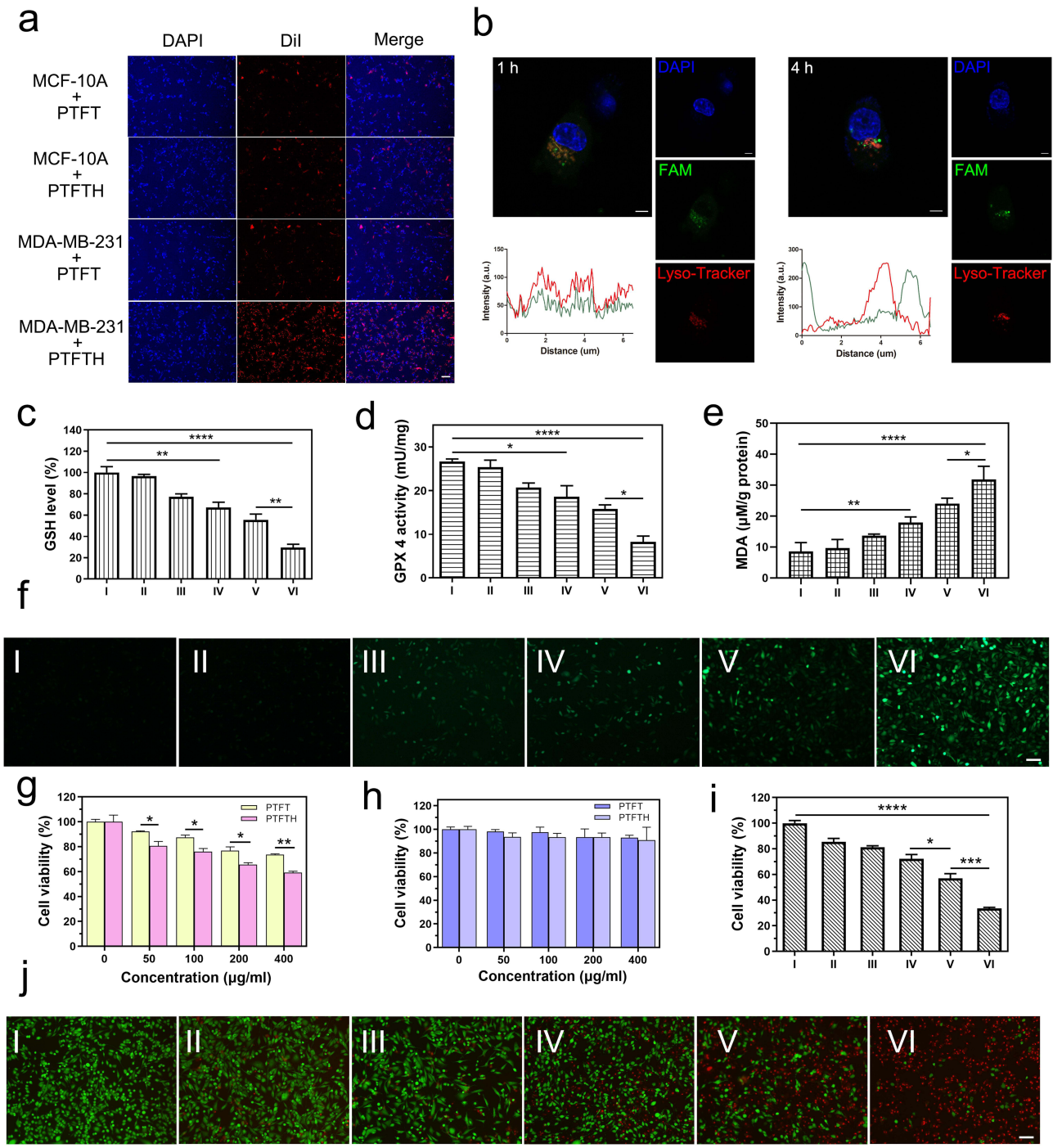

Figure 4 (**a**) Fluorescence images of cellular internalization of DiI-labeled PTFT and PTFTH for MDA-MB-231 cells or MCF-10A cells (scale bar: 100 μm). (**b**) CLSM images and co-localization analyses between FAM-labeled PTFTH and lysosome at different time intervals (scale bar: 5 μm). (**c–e**) GSH, GPX4, and MDA levels in MDA-MB-231 cells under different treatment conditions. (**f**) DCFH-DA determination of intracellular ROS generation in MDA-MB-231 cells after incubation with different samples (scale bar: 100 μm). (**g**) Viability of MDA-MB-231 cells after treated with PTFT or PTFTH at different concentrations. (**h**) Viability of MCF-10A cells after treated with PTFT or PTFTH at different concentrations. (**i**) Viability of MDA-MB-231 cells subjected to various treatments. (**j**) Live/dead cell images of MDA-MB -231 cells treated with different samples (scale bar: 100 μm). (I: Control, II: PFC/TRIM37, III: Fe-TA, IV: PTFT, V: PTFTH, VI: PTFTH + L. Data were presented as mean ± s.d. (n = 3). *p < 0.05, **p < 0.01, ***p < 0.001, ****p < 0.0001.

blue fluorescence was observed in MDA-MB-231 cells with PTFTH incubation, opposite to the negligible overlap for the other three groups, verifying the effective uptake of PTFTH by MDA-MB-231 cells. Subsequently, to evaluate the lysosomal escape capability of PTFTH, the treated MDA-MB-231 cells were stained with LysoTracker Red. With the increase of the incubation time from 1 h to 4 h, the trend of the green fluorescence of FAM-labeled PTFTH and the red

fluorescence of Lyso-Tracker became inconsistent (Figure 4b), indicating the successful lysosomal escape of PTFTH through the traditional "proton-sponge effect". These results implied that PTFTH could specifically enter into tumor cells via CD44 receptor-mediated endocytosis followed by fast escape from acidic lysosomes to release Fe^{3+} and PFC/TRIM37, which was vital for tumor treatment.

Since the released Fe^{3+} could be converted into Fe^{2+} by excess GSH in the TME, we measured the level of intracellular GSH after different treatments. Compared with the PFC/TRIM37 group, an obvious decrease in GSH level was shown in the PTFT group, which illustrated the GSH depletion capacity by Fe^{3+} and the sustained Fenton reaction. In contrast, the PTFTH group was further lower, which was ascribed to the HA-mediated targeting. The GSH depletion capacity was further enhanced in the "PTFTH + L" group, relying on the promotion of the photothermal effect (Figure 4c). GPX4, as a kind of cellular antioxidant enzyme, plays a critical role in lipid redox system. The inadequate supply of GSH directly influenced the activity of GPX4 since GSH is the requisite substrate of GPX4. As shown in Figure 4d, the variation tendency of GPX4 activity in different treated groups was consistent with that of the GSH level. The severe consumption of GSH would destroy the intracellular redox balance and result in the accumulation of excessive ROS. Under this condition, the peroxidation of polyunsaturated fatty acids could form lipid peroxides, leading to ferroptosis. As a final reaction product between free radicals and polyunsaturated fatty acids, malondialdehyde (MDA) could directly reflect the intracellular oxidative stress level. As shown in Figure 4e, cells incubated with PTFTH showed a significantly increased MDA content, which could be further enhanced by photothermal treatment. Besides, 2.7-dichlorofluorescin diacetate (DCFH-DA) was employed to determine the generation of intracellular ROS. As displayed in Figure 4f, no fluorescence was detected in the control and PFC/TRIM37 groups, while a small amount of green fluorescence was found in the Fe-TA and PTFT groups, implying the generation of ROS through Fe^{2+}-mediated Fenton reaction. In contrast, the green fluorescence in the PTFTH group was furtherly enhanced, which was ascribed to the tumor targeting capability of HA. As expected, the cells treated with "PTFTH + L" showed the strongest green fluorescence in comparison with other groups, which was caused by photothermal-triggered ROS generation. In a word, the PTFTH can generate ROS, deplete GSH, inhibit GPX4 activity, and result in the accumulation of lipid peroxides, leading to the tumor cells death through ferroptosis pathway.

To investigate the biosafety of PTFTH, we examined the viabilities of tumor cells (MDA-MB-231 cells) and normal cells (MCF-10A cells) after treatment with PTFTH via CCK-8 assay. As shown in Figure 4g, PTFT and PTFTH displayed slight cytotoxicity to MDA-MB-231 cells with the increase of nanocomplexes concentration, which may be attributed to the GT effect mediated by TRIM37-siRNA and the CDT effect induced by Fe^{2+}. Apparently, PTFTH exhibited much higher cytotoxicity than that of PTFT at the same nanocomplexes concentration, likely due to the HA-mediated targeting to enable enhanced cellular uptake of the nanocomplexes. On the contrary, the viability of MCF-10A cells does not significantly decline in the studied nanocomplexes concentration range under the same conditions, indicating that the PTFT or PTFTH do not induce GT and CDT with a low concentration of H_2O_2 in normal cells (Figure 4h).

Subsequently, the multi-mode therapeutic effect of PTFTH was verified with the MDA-MB-231 cells. As shown in Figure 4i, PFC/TRIM37 decreased the cell viability to about 85%, indicating the occurrence of GT. Besides, Fe-TA decreased the cell viability to about 81%, demonstrating that there was CDT through Fe^{2+}-mediated Fenton reaction. Moreover, the therapeutic effect of PTFT was more robust, and the cell survival rate was reduced to about 72%, indicating that PTFT could induce efficient cell death through GT and CDT. The cell viability in PTFTH group was ulteriorly reduced to 57%, depending on HA-mediated active targeting. The best therapeutic effect of PTFTH under the NIR laser irradiation demonstrated the mutually synergistic effect of PTT, CDT and GT. Furthermore, the multi-mode therapeutic effect of PTFTH under NIR laser irradiation was investigated by fluorescent live/dead cell staining. The results were consistent with the cell viability assay, which displayed the enhanced therapeutic effect with the treatment of PTFTH under NIR laser irradiation (Figure 4j).

Multi-Mode Imaging Capability in vitro

Firstly, the CEUS imaging of PTFTH was investigated. Obvious ultrasonic contrast enhancement was observed in the PTFTH group with various concentrations after laser irradiation (Figure 5a). The PFP liquid-gas phase transition was triggered by the Fe-TA MPNs absorbed light energy, which could provide an explanation for above finding. We quantitatively evaluated the gray scale intensity in the CEUS imaging at different concentrations of PTFTH using

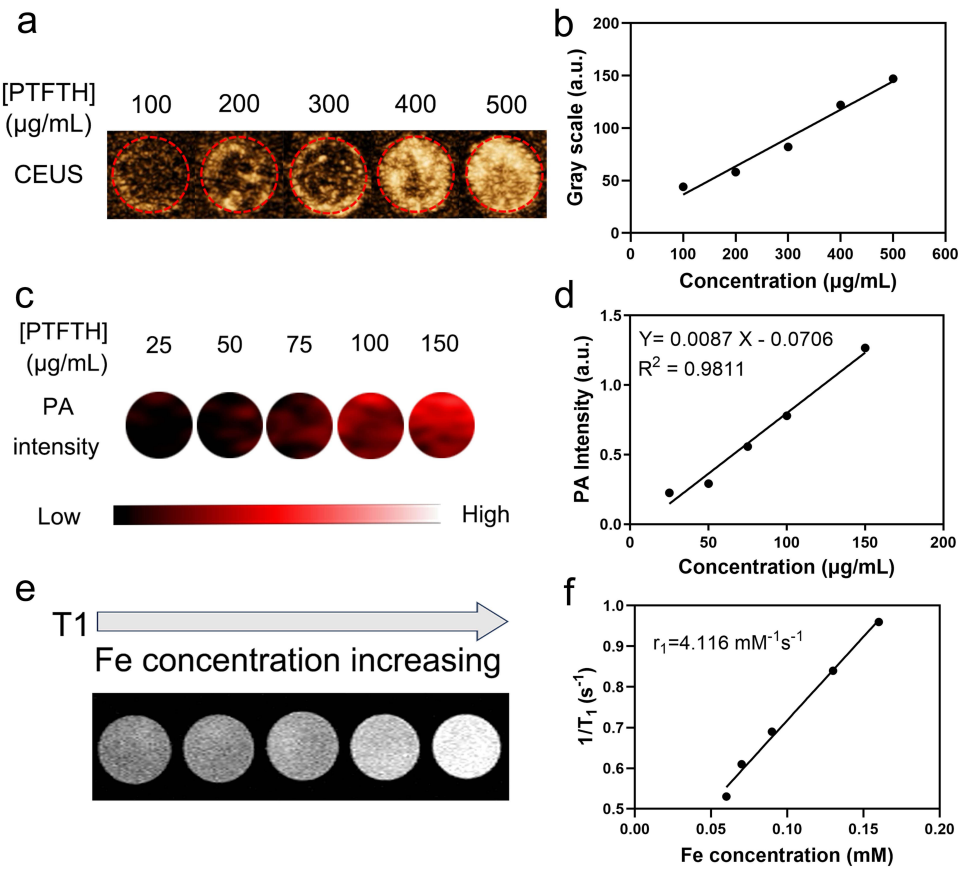

Figure 5 (**a** and **b**) In vitro CEUS imaging intensities of PTFTH with different concentrations. (**c** and **d**) In vitro PA intensities of PTFTH with various concentrations. (**e** and **f**) In vitro T_1-weighted images of PTFTH with different concentrations and the corresponding T_1 relaxation rate (r_1).

ImageJ software (Figure 5b). The results show that the gray scale intensity rose with the increase of PTFTH concentrations.

Subsequently, the PAI capability of PTFTH was explored. The dispersion of PTFTH was subjected to the full wavelength laser scanning (680–970 nm) under the PAI system. It was found that the wavelength at 700–755 nm was the optical biological window for PAI (Figure S7). Considering that longer wavelengths had higher tissue penetrating capability, the PAI was excited and evaluated at 755 nm. Moreover, the photoacoustic signal enhanced proportionally to the increased PTFTH concentrations ranging from 25 μg/mL to 150 μg/mL at 755 nm laser excitation (Figure 5c and d).

Finally, the MRI property of PTFTH was studied. The signal intensity of T_1-weighted MRI was significantly strengthened when the concentration of Fe increased (Figure 5e). Moreover, PTFTH gave the T_1 relaxation rate (r_1) of 4.12 mM^{-1} s^{-1} (Figure 5f), comparable to that of clinically available Gd-based T_1 contrast agents.[48] These results of in vitro experiments show that PTFTH could act as a great contrast agent for high-performance CEUS, PAI and MRI.

Study Limitations

Although satisfactory results have been achieved in vitro, there are still many obstacles to overcome. Firstly, RNA interference technology cannot permanently knock out genes, and thus repeated administration is necessary in vivo, increasing the risk of adverse side effects. In addition, the simplified conditions in vitro could not truly mimic the microenvironment in vivo and the behavior of particles migration may be different. Therefore, further exploration is needed for the application in vivo.

Conclusion

In summary, we developed a TME-activated and NIR-driven PTFTH nanoplatform by coating the Fe-TA MPNs on the surface of TRIM37-siRNA loaded PFC nanodroplets and further modifying them with HA for tumor-specific MPTT/GT/Ferroptosis synergistic therapy in vitro. The modification of HA effectively increased the uptake of PTFTH by tumor cells via CD44 receptor-mediated endocytosis. In addition, both HA coating and Fe-TA MPNs acted as guards to avoid the premature release of siRNA, contributing to the HAase/pH dual-responsive release of Fe^{3+} and siRNA at tumor sites. The released Fe^{3+} could be converted to Fe^{2+} by intracellular GSH, which then converted endogenous H_2O_2 into toxic •OH for CDT. Benefiting from the excellent photothermal conversion efficiency (36.6%), PTFTH could serve as an effective photothermal agent for MPTT. Meanwhile, the generated local hyperthermia not only enhanced CDT efficacy via accelerating the Fe^{2+}-mediated Fenton reaction but also accelerated siRNA release for GT. The depletion of GSH and accumulation of •OH synergistically enhanced intracellular oxidative stress, inducing extensive tumor cell ferroptosis. Moreover, as excellent CEUS, PAI, and MRI multimodal contrast agents, PTFTH acted as multifunctional theranostic agents could achieve multimodal imaging guidance for synergistic MPTT/GT/Ferroptosis strategy. Taken together, PTFTH is a promising tool for future clinical cancer therapy.

Acknowledgments

This work was supported by the National Natural Science Foundation of China (Grant No. 82171953).

Author Contributions

All authors made a significant contribution to the work reported, whether that is in the conception, study design, execution, acquisition of data, analysis and interpretation, or in all these areas; took part in drafting, revising or critically reviewing the article; gave final approval of the version to be published; have agreed on the journal to which the article has been submitted; and agree to be accountable for all aspects of the work.

Disclosure

The authors declare that no competing interest exists in this work.

References

1. Siegel RL, Miller KD, Fuchs HE, et al. Cancer statistics, 2022. *CA Cancer J Clin*. 2022;72(1):7–33. doi:10.3322/caac.21708
2. Lee KL, Kuo YC, Ho YS, et al. Triple-negative breast cancer: current understanding and future therapeutic breakthrough targeting cancer stemness. *Cancers*. 2019;11(9):1334.
3. Denkert C, von Minckwitz G, Darb-Esfahani S, et al. Tumour-infiltrating lymphocytes and prognosis in different subtypes of breast cancer: a pooled analysis of 3771 patients treated with neoadjuvant therapy. *Lancet Oncol*. 2018;19(1):40–50. doi:10.1016/S1470-2045(17)30904-X
4. Sun X, Wang M, Wang M, et al. Metabolic reprogramming in triple-negative breast cancer. *Front Oncol*. 2020;10:428. doi:10.3389/fonc.2020.00428
5. Fan XX, Pan HD, Li Y, et al. Novel therapeutic strategy for cancer and autoimmune conditions: modulating cell metabolism and redox capacity. *Pharmacol Ther*. 2018;191:148–161. doi:10.1016/j.pharmthera.2018.06.010
6. Guan G, Zhang C, Liu H, et al. Ternary alloy PtWMn as a Mn nanoreservoir for high-field MRI monitoring and highly selective ferroptosis therapy. *Angew Chem Int Ed Engl*. 2022;61(31):e202117229. doi:10.1002/anie.202117229
7. Chen H, Luo X, Huang Q, et al. Platelet membrane fusion liposome loaded with type I AIE photosensitizer to induce chemoresistance cancer pyroptosis and immunogenic cell death for enhancing cancer immunotherapy. *Chem Eng J*. 2023;476:146276. doi:10.1016/j.cej.2023.146276
8. Hassannia B, Vandenabeele P, Vanden Berghe T. Targeting ferroptosis to iron out cancer. *Cancer Cell*. 2019;35(6):830–849. doi:10.1016/j.ccell.2019.04.002
9. Zhang C, Liu X, Jin S, et al. Ferroptosis in cancer therapy: a novel approach to reversing drug resistance. *Mol Cancer*. 2022;21(1):47. doi:10.1186/s12943-022-01530-y
10. Cao F, Sang Y, Liu C, et al. Self-adaptive single-atom catalyst boosting selective ferroptosis in tumor cells. *ACS Nano*. 2022;16(1):855–868. doi:10.1021/acsnano.1c08464
11. Wan X, Song L, Pan W, et al. Tumor-targeted cascade nanoreactor based on metal-organic frameworks for synergistic ferroptosis-starvation anticancer therapy. *ACS Nano*. 2020;14(9):11017–11028. doi:10.1021/acsnano.9b07789
12. Xu Y, Guo Y, Zhang C, et al. Fibronectin-coated metal-phenolic networks for cooperative tumor chemo-/chemodynamic/immune therapy via enhanced ferroptosis-mediated immunogenic cell death. *ACS Nano*. 2022;16(1):984–996. doi:10.1021/acsnano.1c08585
13. Zhu D, Ling R, Chen H, et al. Biomimetic copper single-atom nanozyme system for self-enhanced nanocatalytic tumor therapy. *Nano Res*. 2022;15(8):7320–7328. doi:10.1007/s12274-022-4359-6
14. Ning S, Zhang T, Lyu M, et al. A type I AIE photosensitiser-loaded biomimetic nanosystem allowing precise depletion of cancer stem cells and prevention of cancer recurrence after radiotherapy. *Biomaterials*. 2023;295:122034. doi:10.1016/j.biomaterials.2023.122034

15. Ning S, Lyu M, Zhu D, et al. Type-I AIE photosensitizer loaded biomimetic system boosting cuproptos is to inhibit breast cancer metastasis and rechallenge. *ACS Nano*. 2023;17(11):10206–10217. doi:10.1021/acsnano.3c00326
16. Zhu D, Zhang T, Li Y, et al. Tumor-derived exosomes co-delivering aggregation-induced emission luminogens and proton pump inhibitors for tumor glutamine starvation therapy and enhanced type-I photodynamic therapy. *Biomaterials*. 2022;283:121462. doi:10.1016/j.biomaterials.2022.121462
17. Zhang N, Ping W, Rao K, et al. Biomimetic copper-doped polypyrrole nanoparticles induce glutamine metabolism inhibition to enhance breast cancer cuproptosis and immunotherapy. *J Control Release*. 2024;371:204–215. doi:10.1016/j.jconrel.2024.05.045
18. Odda AH, Cheang TY, Alesary HF, et al. A multifunctional alpha-Fe(2)O(3)@PEDOT core-shell nanoplatform for gene and photothermal combination anticancer therapy. *J Mater Chem B*. 2022;10(9):1453–1462. doi:10.1039/D1TB02625A
19. Lu W, Zhang G, Zhang R, et al. Tumor site-specific silencing of NF-kappaB p65 by targeted hollow gold nanosphere-mediated photothermal transfection. *Cancer Res*. 2010;70(8):3177–3188. doi:10.1158/0008-5472.CAN-09-3379
20. Ambrosio L, Argenziano M, Cucci MA, et al. Carbosilane dendrimers loaded with siRNA targeting Nrf2 as a tool to overcome cisplatin chemoresistance in bladder cancer cells. *Antioxidants*. 2020;9(10):993. doi:10.3390/antiox9100993
21. de Fougerolles A, Vornlocher HP, Maraganore J, et al. Interfering with disease: a progress report on siRNA-based therapeutics. *Nat Rev Drug Discov*. 2007;6(6):443–453. doi:10.1038/nrd2310
22. Liu Y, Zhou Y, Xu J, et al. Ultrasound molecular imaging-guided tumor gene therapy through dual-targeted cationic microbubbles. *Biomater Sci*. 2021;9(7):2454–2466. doi:10.1039/D0BM01857K
23. Zhou Y, Gu H, Xu Y, et al. Targeted antiangiogenesis gene therapy using targeted cationic microbubbles conjugated with CD105 antibody compared with untargeted cationic and neutral microbubbles. *Theranostics*. 2015;5(4):399–417. doi:10.7150/thno.10351
24. Chin LS, Lim M, Hung TT, et al. Perfluorodecalin nanocapsule as an oxygen carrier and contrast agent for ultrasound imaging. *RSC Adv*. 2014;4(25):13052. doi:10.1039/c3ra47595f
25. Zhang Z, Taylor M, Kaval N, et al. Phase-transition temperature of gold-nanorod-coated nanodroplets to microbubbles by pulsed laser. *J Phys Chem A*. 2019;123(23):4844–4852. doi:10.1021/acs.jpca.9b02566
26. Liu J, Shang T, Wang F, et al. Low-intensity focused ultrasound (LIFU)-induced acoustic droplet vaporization in phase-transition perfluoropentane nanodroplets modified by folate for ultrasound molecular imaging. *Int J Nanomed*. 2017;12:911–923. doi:10.2147/IJN.S122667
27. Yuan Z, Demith A, Stoffel R, et al. Light-activated doxorubicin-encapsulated perfluorocarbon nanodroplets for on-demand drug delivery in an in vitro angiogenesis model: comparison between perfluoropentane and perfluorohexane. *Colloids Surf B Biointerfaces*. 2019;184:110484. doi:10.1016/j.colsurfb.2019.110484
28. Park S, Son G. Numerical study of the effect of liquid compressibility on acoustic droplet vaporization. *Ultrason Sonochem*. 2021;79:105769. doi:10.1016/j.ultsonch.2021.105769
29. Fan CH, Lin YT, Ho YJ, et al. Spatial-temporal cellular bioeffects from acoustic droplet vaporization. *Theranostics*. 2018;8(20):5731–5743. doi:10.7150/thno.28782
30. Singh R, Husseini GA, Pitt WG. Phase transitions of nanoemulsions using ultrasound: experimental observations. *Ultrason Sonochem*. 2012;19(5):1120–1125. doi:10.1016/j.ultsonch.2012.02.005
31. Chen Q, Yu J, Kim K. Review: optically-triggered phase-transition droplets for photoacoustic imaging. *Biomed Eng Lett*. 2018;8(2):223–229. doi:10.1007/s13534-018-0069-0
32. Bhatnagar S, Gazin C, Chamberlain L, et al. TRIM37 is a new histone H2A ubiquitin ligase and breast cancer oncoprotein. *Nature*. 2014;516(7529):116–120. doi:10.1038/nature13955
33. Przanowski P, Lou S, Tihagam RD, et al. Oncogenic TRIM37 links chemoresistance and metastatic fate in triple-negative breast cancer. *Cancer Res*. 2020;80(21):4791–4804. doi:10.1158/0008-5472.CAN-20-1459
34. Liu T, Zhang M, Liu W, et al. Metal ion/tannic acid assembly as a versatile photothermal platform in engineering multimodal nanotheranostics for advanced applications. *ACS Nano*. 2018;12(4):3917–3927. doi:10.1021/acsnano.8b01456
35. Jiang Y, Zhao X, Huang J, et al. Transformable hybrid semiconducting polymer nanozyme for second near-infrared photothermal ferrotherapy. *Nat Commun*. 2020;11(1):1857. doi:10.1038/s41467-020-15730-x
36. Kim J, Kim J, Jeong C, et al. Synergistic nanomedicine by combined gene and photothermal therapy. *Adv Drug Deliv Rev*. 2016;98:99–112. doi:10.1016/j.addr.2015.12.018
37. Wu M, Xiong H, Zou H, et al. A laser-activated multifunctional targeted nanoagent for imaging and gene therapy in a mouse xenograft model with retinoblastoma Y79 cells. *Acta Biomater*. 2018;73:355. doi:10.1016/j.actbio.2018.03.058
38. Sungur S, Uzar A. Investigation of complexes tannic acid and myricetin with Fe(III). *Spectrochim Acta A Mol Biomol Spectrosc*. 2008;69(1):225–229. doi:10.1016/j.saa.2007.03.038
39. Zeng F, Tang L, Zhang Q, et al. Coordinating the mechanisms of action of ferroptosis and the photothermal effect for cancer theranostics. *Angew Chem Int Ed*. 2022;61(13): e202112925. doi:10.1002/anie.202112925
40. Sun S-P, C-J L, Sun J-H, et al. Decolorization of an azo dye Orange G in aqueous solution by Fenton oxidation process: effect of system parameters and kinetic study. *J Hazard Mater*. 2009;161(2–3):1052–1057. doi:10.1016/j.jhazmat.2008.04.080
41. Hessel CM, Pattani VP, Rasch M, et al. Copper selenide nanocrystals for photothermal therapy. *Nano Lett*. 2011;11(6):2560–2566. doi:10.1021/nl201400z
42. Tian Q, Jiang F, Zou R, et al. Hydrophilic Cu9S5 nanocrystals: a photothermal agent with a 25.7% heat conversion efficiency for photothermal ablation of cancer cells in vivo. *ACS nano*. 2011;5(12):9761–9771. doi:10.1021/nn203293t
43. Zeng J, Goldfeld D, Xia Y. A plasmon-assisted optofluidic (PAOF) system for measuring the photothermal conversion efficiencies of gold nanostructures and controlling an electrical switch. *Angew Chem*. 2013;52(15):4169–4173. doi:10.1002/anie.201210359
44. Wang Z, Jiang S, Li S, et al. Targeted galectin-7 inhibition with ultrasound microbubble targeted gene therapy as a sole therapy to prevent acute rejection following heart transplantation in a rodent model. *Biomaterials*. 2020;263:120366. doi:10.1016/j.biomaterials.2020.120366
45. Y-J H, Chang Y-C, Yeh C-K. Improving nanoparticle penetration in tumors by vascular disruption with acoustic droplet vaporization. *Theranostics*. 2016;6(3):392–403. doi:10.7150/thno.13727
46. Mo S, Coussios -C-C, Seymour L, et al. Ultrasound-enhanced drug delivery for cancer. *Expert Opin Drug Deliv*. 2012;9(12):1525–1538. doi:10.1517/17425247.2012.739603

47. Tian Y, Liu Z, Tan H, et al. New aspects of ultrasound-mediated targeted delivery and therapy for cancer. *Int J Nanomed*. 2020;15:401–418. doi:10.2147/IJN.S201208
48. Shen Y, Goerner FL, Snyder C, et al. T1 relaxivities of gadolinium-based magnetic resonance contrast agents in human whole blood at 1.5, 3, and 7 T. *Invest Radiol*. 2015;50(5):330–338. doi:10.1097/RLI.0000000000000132